Death-specific protein in a marine diatom regulates photosynthetic responses to iron and light availability

Kimberlee Thamatrakoln[a,1], Benjamin Bailleul[a], Christopher M. Brown[a], Maxim Y. Gorbunov[a], Adam B. Kustka[b], Miguel Frada[a,c], Pierre A. Joliot[d], Paul G. Falkowski[a], and Kay D. Bidle[a,1]

[a]Environmental Biophysics and Molecular Ecology Laboratory, Institute of Marine and Coastal Sciences, Rutgers University, New Brunswick, NJ 08901; [b]Department of Earth and Environmental Sciences, Rutgers University, Newark, NJ 07102; [c]Plant Sciences Department, The Weizmann Institute of Science, Rehovot 76100, Israel; and [d]Institut de Biologie Physico-Chimique, Unité Mixte de Recherche 7141, Centre National de la Recherche Scientifique and Université Pierre et Marie Curie–Université Paris 6, 75005 Paris, France

Edited by David M. Karl, University of Hawaii, Honolulu, HI, and approved October 25, 2013 (received for review March 12, 2013)

Diatoms, unicellular phytoplankton that account for ∼40% of marine primary productivity, often dominate coastal and open-ocean upwelling zones. Limitation of growth and productivity by iron at low light is attributed to an elevated cellular Fe requirement for the synthesis of Fe-rich photosynthetic proteins. In the dynamic coastal environment, Fe concentrations and daily surface irradiance levels can vary by two to three orders of magnitude on short spatial and temporal scales. Although genome-wide studies are beginning to provide insight into the molecular mechanisms used by diatoms to rapidly respond to such fluxes, their functional role in mediating the Fe stress response remains uncharacterized. Here, we show, using reverse genetics, that a death-specific protein (DSP; previously named for its apparent association with cell death) in the coastal diatom *Thalassiosira pseudonana* (TpDSP1) localizes to the plastid and enhances growth during acute Fe limitation at subsaturating light by increasing the photosynthetic efficiency of carbon fixation. Clone lines overexpressing TpDSP1 had a lower quantum requirement for growth, increased levels of photosynthetic and carbon fixation proteins, and increased cyclic electron flow around photosystem I. Cyclic electron flow is an ATP-producing pathway essential in higher plants and chlorophytes with a heretofore unappreciated role in diatoms. However, cells under replete conditions were characterized as having markedly reduced growth and photosynthetic rates at saturating light, thereby constraining the benefits afforded by overexpression. Widespread distribution of DSP-like sequences in environmental metagenomic and metatranscriptomic datasets highlights the presence and relevance of this protein in natural phytoplankton populations in diverse oceanic regimes.

high light | photosynthesis | nutrient limitation

Iron (Fe) limitation profoundly affects phytoplankton productivity by decreasing the efficiency of photochemical conversion of light into chemical bond energy (1). Fe enrichments in high-nutrient, low-chlorophyll areas of the Southern Ocean, the Equatorial Pacific, and the North Pacific (2) as well as coastal upwelling zones (3) result in large diatom blooms by allowing increased photosynthetic capacity and higher growth rates. In some diatoms, tolerance of chronically low Fe is aided by efficient Fe uptake systems (4), intracellular Fe storage (5, 6), or biochemical alteration of the photosynthetic Fe demand through decreased expression of the Fe-rich photosystem I (PSI) and cytochrome b_6f components (7, 8). Comparatively little is known about how diatoms deal with episodic Fe and light availability. In the highly dynamic coastal environment, Fe concentrations and daily surface irradiance levels can vary by two to three orders of magnitude (3, 9) on short spatial and temporal scales. Diatoms that thrive in these environments must, therefore, possess sophisticated cellular mechanisms to rapidly respond to such fluxes. Although genome-wide studies on the response of diatoms to acute and chronic Fe limitations have revealed a variety of Fe-responsive pathways and associated genes (7, 10, 11), their functional roles in mediating the response have yet to be understood.

Using whole-genome comparative transcriptomics and diagnostic biochemistry, we previously identified two closely related genes whose expression was induced by Fe limitation and oxidative stress in the coastal marine diatom, *Thalassiosira pseudonana* (11). Their associated protein sequences had strongest homology to so-called death-specific proteins (DSPs) from the diatom *Skeletonema costatum* (ScDSP1) (12) and thus, were denoted *T. pseudonana* DSP1 (TpDSP1; BLASTp e value $< 1 \times 10^{-76}$) and TpDSP2 (BLASTp e value $< 3 \times 10^{-26}$) (Fig. S1*A*). *ScDSP1* expression is induced by senescence, low light, chemical inhibition of photosystem II (PSII)/cytochrome b_6f, and high intracellular levels of nitric oxide (12, 13). Similar to ScDSP1, both TpDSP proteins possess a predicted membrane-spanning region and a pair of calcium (Ca^{2+}) binding EF-hand motifs (Fig. S1*A*). The DSP family has closest similarity to proteins associated with Ca^{2+}-dependent signal transduction cascades, including calmodulin, a Ca^{2+}-dependent mitochondrial carrier protein, and Ca^{2+}-dependent protein kinases (BLASTp e value $< 1 \times 10^{-4}$).

In silico analysis gave conflicting predictions for the subcellular localization of TpDSP1. Although HECTAR (14) and ChloroP (15) targeted TpDSP1 to other locations (score = 0.6408 and 0.490, respectively), TargetP (16) and LumenP (17) predicted chloroplast localization (reliability class = 5 and score = 0.978, respectively). For comparison, TpDSP2 was consistently predicted

Significance

Diatoms are unicellular eukaryotic phytoplankton responsible for nearly one-half of total marine primary productivity. We identified a plastid-targeted protein in the coastal diatom *Thalassiosira pseudonana* (TpDSP1) that enhances growth during iron limitation under low light. Clone lines overexpressing TpDSP1 had lower quantum requirements for growth, increased levels of photosynthetic and carbon fixation proteins, and increased cyclic electron flow around photosystem I, an energy-producing pathway with a heretofore unappreciated role in diatoms. At the same time, clones growing under replete conditions had markedly reduced growth and photosynthetic rates under high light, suggesting that, although TpDSP1 confers a competitive advantage under iron limitation, cells walk an ecological tightrope through the regulation of this protein.

Author contributions: K.T., P.G.F., and K.D.B. designed research; K.T., B.B., C.M.B., M.Y.G., A.B.K., M.F., and P.A.J. performed research; K.T., B.B., C.M.B., M.Y.G., A.B.K., P.A.J., P.G.F., and K.D.B. analyzed data; and K.T., B.B., P.G.F., and K.D.B. wrote the paper.

The authors declare no conflict of interest.

This article is a PNAS Direct Submission.

Freely available online through the PNAS open access option.

[1]To whom correspondence may be addressed. E-mail: thamat@marine.rutgers.edu or bidle@marine.rutgers.edu.

This article contains supporting information online at www.pnas.org/lookup/suppl/doi:10.1073/pnas.1304727110/-/DCSupplemental.

to be nonchloroplastic and nonmitochondrial, with a predicted signal peptide cleavage site between amino acids 26 and 27. Given the induction of *DSPs* by Fe limitation, oxidative stress (11), and low light (13) and its potential plastid localization, we hypothesized that TpDSP1 plays a critical role in the photosynthetic response to Fe and light availability.

In this study, we used a reverse genetics approach to explore the functional role of TpDSP1 in *T. pseudonana*. Because methods for generating knockout or silencing mutants do not currently exist in this organism, we overexpressed TpDSP1 in its native cellular background to determine its role in the response to Fe and light availability. Our results show that overexpression of TpDSP1 enhances growth under Fe limitation at subsaturating light by modulating photosynthetic electron transport but that these benefits are constrained by the cost of impaired growth at high irradiance levels.

Results and Discussion

TpDSP1 was overexpressed in *T. pseudonana* as a C-terminal fusion with GFP (Fig. S1*B*). Immunoblot (Fig. 1*A*) and flow cytometry analysis of GFP fluorescence (Fig. 1*B*) confirmed overexpression in three independent clone lines (denoted 18–58, 18–31, and 18–53). The three clones differed in the degree to which TpDSP1-GFP was overexpressed, with clone 18–58 having the highest levels of fusion protein expression (Fig. 1*A*) and GFP fluorescence (in both mean fluorescence intensity and the percent of GFP-positive cells in the culture) (Fig. 1*B*). Quantitative, reverse-transcriptase PCR (qRT-PCR) showed a 4.8-fold increase in *DSP* mRNA expression compared with wild-type (WT). Cell extracts challenged with polyclonal peptide antibodies designed against TpDSP1 and generated in two rabbits further confirmed overexpression of TpDSP1 protein. Although antisera from each rabbit displayed differential cross-reactivity with endogenous DSP and the TpDSP1-GFP fusion protein, peptide competition assays confirmed that both antisera were specific to TpDSP1 (Fig. S2). Taken together, qRT-PCR, flow cytometry, and GFP immunoblot data showed that TpDSP1 was overexpressed on both the mRNA and protein levels in these transgenic clone lines.

Confocal laser microscopy localized TpDSP1 to the plastid (Fig. 1*C*), confirming the in silico prediction by TargetP and LumenP and refuting HECTAR and ChloroP. Plastid targeting in diatoms depends on a unique bipartite sequence that consists of a signal peptide followed by a transit peptide (18). Although generally conserved, both in vivo experiments with modified presequences and large-scale targeted sequencing projects have revealed deviations that still result in chloroplast targeting (19, 20), showing that, although useful, in silico predictions are not always correct. We confirmed that localization was not an artifact of overexpression, because a GFP-only expressing clone possessed cytoplasmic GFP fluorescence (Fig. 1*C*).

Physiologically, overexpression of TpDSP1 greatly enhanced cellular fitness in the three clone lines under Fe limitation at subsaturating irradiance; as evidenced by a significant increase in the specific growth rate (μ) over WT (Fig. 1 *D* and *E* and Table S1), which consistently occurred 2–3 d after the shift from Fe replete to Fe-free media (i.e., acute Fe limitation; hereafter referred to as Fe limitation). The enhanced low Fe fitness was not associated with an increase in the maximum photochemical quantum yield of PSII (F_v/F_m) (Fig. 1*D*) or increased expression of TpDSP1-GFP under Fe limitation (Fig. 1*D*, *Inset*). Enhanced growth was also not caused by the presence of GFP, given μ of the GFP-only expressing clone was identical to that of WT under Fe limitation. Moreover, overexpression of TpDSP1 did not confer an advantage to growth under nutrient replete conditions (Table S1) or nitrogen limitation ($\mu = 0.19\ d^{-1}$), further implicating its connection to Fe stress. Although clones 18–31 and 18–53 expressed the fusion protein to a lesser degree than clone 18–58 (Fig. 1*A*), all three displayed similar phenotypes under Fe limitation (Fig. 1*E*), suggesting that there may be a threshold level of expression, above which there are no additional benefits.

Given the identical phenotypes under Fe limitation, we chose clone 18–58 for additional detailed characterization, because it displayed the highest levels of GFP expression and mean fluorescence intensity. For simplicity, clone 18–58 will hereafter be referred to as TpDSP1-GFP. Unlike in acute Fe limitation, TpDSP1 overexpression did not enhance steady-state growth under a range of Fe concentrations (Fig. S3*A*). Furthermore, there was no significant difference between cellular Fe quota and steady-state uptake rates between WT and TpDSP1-GFP at any of the Fe′ tested (Fig. S3 *B–D*), indicating that TpDSP1 overexpression did not enhance intracellular storage or uptake of Fe. These findings demonstrate the increased fitness conferred by overexpressing TpDSP1 was specific to acute Fe limitation and not because of fundamentally altered Fe metabolism.

In photoautotrophs, Fe limitation leads to chlorosis and down-regulation of photosynthesis. Under replete conditions, TpDSP1-GFP had 26% less chlorophyll *a* (Chl *a*) per cell than WT (Table

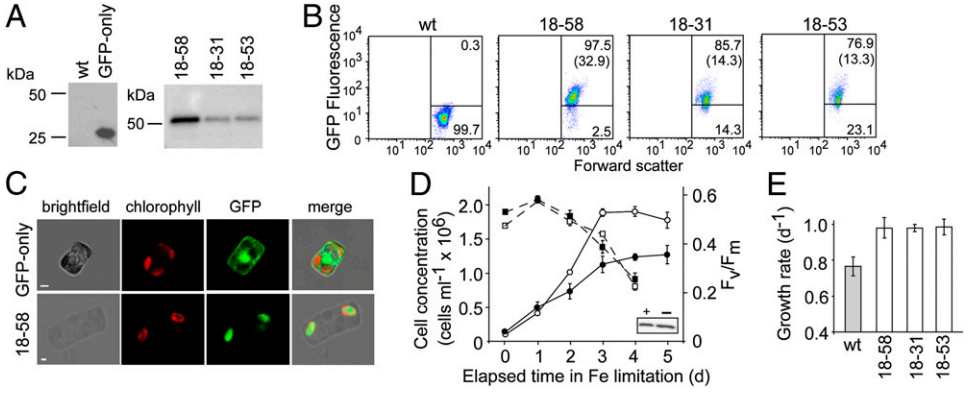

Fig. 1. Characterization of TpDSP1 transgenic clone lines. (*A*) GFP immunoblot of WT, a GFP-only expressing clone, and three TpDSP1 overexpressing clone lines (18–58, 18–31, and 18–53) showed cross-reactivity with GFP (27 kDa) and an ~50-kDa protein in the TpDSP1 overexpressing cells, consistent with the expected size of the fusion protein. Cells were harvested under exponentially growing replete conditions. (*B*) Flow cytometry of GFP fluorescence. Percent of total cells in each gate (>10,000 cells) is shown with the mean GFP fluorescence intensity of the GFP-positive population (upper right quadrant) in parentheses. (*C*) Light and confocal microscopy of GFP-only expressing cells and a representative TpDSP1 overexpressing cell. Brightfield, chlorophyll autofluorescence, GFP fluorescence, and a merged image are shown. (Scale bar: 1 μm.) (*D*) Time course of acute Fe limitation in WT and clone 18–58. Solid lines and circles represent cell concentration; dashed lines and squares are F_v/F_m (closed symbols, WT; open symbols, 18–58). The mean ± SD for triplicate cultures is shown. Data are shown for one experiment but representative of eight independent experiments (each with two to three biological replicates), in which the average μ was 0.81 ± 0.22 and 0.56 ± 0.20 d^{-1} for TpDSP1-GFP and WT, respectively [Student *t* test, $t(7) = 2.4$, $P = 2.6 \times 10^{-5}$]. *Inset* shows an immunoblot of 18–58 grown in replete (+) or Fe-limited (–) conditions. (*E*) Mean specific growth rate ± SD of triplicate cultures of WT and the three TpDSP overexpressing clone lines under acute Fe limitation.

S1), suggesting that overexpression of TpDSP1 affected Chl biosynthesis. Under Fe limitation, Chl *a* per cell in WT decreased 38% but remained unchanged in TpDSP1-GFP (Table S1). Quantitative immunoblots (21) were used to determine if overexpression of TpDSP1 simultaneously altered the levels or relative ratios of key components of photosynthesis (PSII, cytochrome b_6f, PSI, and ATP synthase) and carbon fixation (RuBisCO). Under replete conditions, both WT and TpDSP1-GFP maintained similar levels of these components at a ratio of ~2:1:1:1:12 for PSII:cytb_6f:PSI:ATPSynthase:RuBisCO (Fig. S4 and Table S1). Acute Fe limitation in WT led to an approximately twofold decrease in the abundance of each component, but notably, the relative stoichiometry remained unchanged. TpDSP1-GFP also maintained the 2:1:1:1:12 ratio under Fe limitation, but the overall abundance of each component was 1.4- to 2-fold higher than in WT. The electrochromic shift (ECS) signal, a light-driven absorbance change driven by the shift in the absorption spectrum of some photosynthetic pigments in the presence of a photosynthesis-driven electric field across the thylakoid membrane, confirmed that the PSII:PSI ratios represent active reaction centers (Fig. 2*C*). Hence, although TpDSP1 overexpression did not alter the architecture of the photosynthetic apparatus, it did enable cells to maintain elevated levels despite Fe limitation, thereby supporting higher growth rates.

The increased growth rate of TpDSP1-GFP could also be explained by an increase in energy use efficiency and higher carbon fixation rates. The quantum requirement for growth ($1/\varphi_\mu$) (*SI Materials and Methods*) under acute Fe limitation was approximately twofold lower in TpDSP1-GFP compared with WT (29 ± 6 and 65 ± 15 mol quanta mol C^{-1}, respectively), indicating that TpDSP1-GFP was more efficient at converting light into chemical bond energy. Lower quantum requirements can be attributed to either an increase in linear electron flow (LEF), expressed as an electron transport rate (ETR), or increased PSII subunits, with the product (ETR × PSII) of the two yielding the per-cell carbon fixation rate. The maximum ETR per PSII (P_{max}), the saturation irradiance for photosynthesis (E_k), the maximum efficiency of PSII (F_v/F_m), and the functional cross-section of PSII (σ_{PSII}) were not significantly different between TpDSP1-GFP and WT (Table S1). However, although ETR per PSII was similar, the approximately twofold higher cellular PSII levels in TpDSP1-GFP under Fe limitation (Fig. S4*A* and Table S1) translate into an approximately twofold higher ETR per cell.

An increased ETR would logically result in a higher ATP demand to support both carbon fixation and other ATP-dependent cellular processes associated with higher growth rates. DSPs are restricted to the red algal lineage (12) and have the highest similarity to Ca^{2+} binding proteins, in part because of the highly conserved nature of the Ca^{2+} binding EF-hand motif (a motif found in numerous proteins involved in a wide array of cellular functions, many of which are unrelated to each other). However, we found partial and distant similarity to the thylakoid-associated proton gradient regulator-5 (PGR5; BLASTp e value < 4×10^{-4}) protein found in higher plants. Multiple sequence alignment between DSP and PGR5 shows amino acid similarity over ~140 aa that are located outside the EF-hand motif. Conservation of a critical glycine residue (Fig. S5), the substitution of which in PGR5 (position 130) renders the protein unstable and nonfunctional (22), was also shared. PGR5, in conjunction with the transmembrane protein PGRL1, plays a critical role in regulating cyclic electron flow (CEF) around PSI (22, 23), an alternate pathway of electron transport essential to photosynthesis (24). During CEF, reduced PSI acceptors shuttle electrons to plastoquinone, which then reduces $P700^+$ through cytochrome b_6f (25). This process contributes to the generation of a proton gradient for ATP production, and therefore, it plays a key role in adjusting the ATP:NADPH ratio required for carbon fixation and preventing overreduction of the chloroplast, especially during stress (26). Although documented to play a critical role in higher plants and chlorophytes (24), the incidence and importance of CEF around PSI in diatoms have not been well-characterized. We directly measured CEF around PSI using ECS-based measurements of WT and TpDSP1-GFP. The measurement of a light-induced proton gradient, in conditions where PSII was inhibited (*Materials and Methods*), suggests that CEF can potentially generate ATP under normal, unstressed conditions in *T. pseudonana*. The similar basal levels of CEF under replete conditions (Fig. 2*D*) between WT and TpDSP1-GFP further suggest that, in an unstressed cell, overexpression of TpDSP1 alone does not a priori facilitate higher rates of CEF, likely because additional ATP is not required. Under Fe limitation, however, TpDSP1 overexpression facilitated 61 ± 15% higher CEF around PSI, over replete conditions (Fig. 2*D*). The saturation curves of the PSI-associated photoacoustic response showed that this increase was not because of an increase in PSI light harvesting capacity (σ_{PSI}) (Table S1).

Collectively, these data show that overexpression of TpDSP1 confers a photochemical advantage under Fe limitation, whereby cells maintain the abundance of key components of the photosynthetic apparatus and have increased LEF and CEF around PSI (Fig. 3*A*). This finding is analogous to the PGR5/PGRL1 complex modulating LEF and CEF around PSI in the green plastid lineage (22, 23). We hypothesize that DSP plays a similar role of regulating the proton gradient across the thylakoid membrane in organisms in the red plastid lineage. Notably, the genomes of *T. pseudonana*, *Phaeodactylum tricornutum*, *Fragilariopsis cylindrus*, and *Emiliania huxleyi* each contain a predicted gene with higher similarity to PGR5 (BLASTp e values ranging from 5×10^{-16} to 6×10^{-27}) (Fig. S5) than DSPs (BLASTp e value < 4×10^{-4}), indicating that DSPs may not be true PGR5

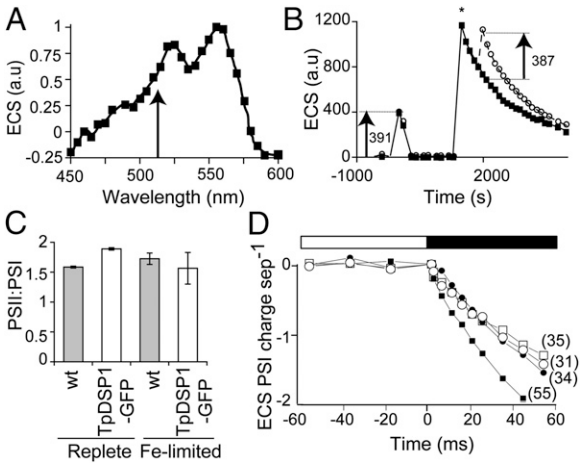

Fig. 2. ECS signal-based measurements. (*A*) The light minus dark ECS signal in WT was measured 500 ms after a saturating laser flash. Subsequent ECS-based experiments were done at 513 nm (denoted by the arrow). (*B*) Comparison of the flash-induced ECS signal in dark adapted cells and after the building of a strong electric field by six consecutive flashes (represented by the asterisk). The virtually identical values (shown next to the arrows) show that the ECS signal is proportional to the electric field. (*C*) Active PSII:PSI. The mean ± SD for two biological replicates is shown. (*D*) PSI cyclic electron transfer rate in PSII-inhibited cultures of WT (circles) and TpDSP1-GFP (squares) under replete (open symbols) and Fe-limited (closed symbols) conditions. Data are from a single experiment but representative of two independent replicates. After a steady-state baseline proton gradient is reached in the light (white bar, 340 μmol photons m^{-2} s^{-1}), the slope of the ECS signal in the dark (black bar) represents the rate of the CEF-related proton transport in the light. The rate of CEF (charge separations $seconds^{-1}$ PSI^{-1}) is shown in parentheses.

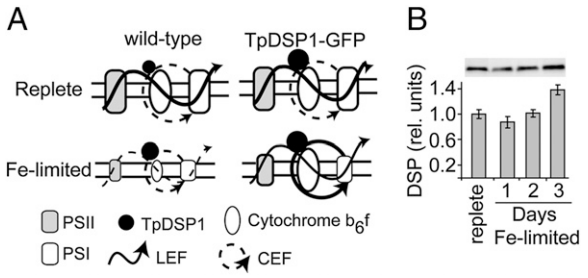

Fig. 3. Model of electron transport and photosynthetic protein levels. (*A*) Schematic of electron transport and photosynthetic components in WT (*Left*) and TpDSP1-GFP (*Right*) under replete (*Upper*) or Fe-limiting (*Lower*) conditions. The thylakoid membrane is depicted with PSII (shaded rectangle), Cyt b_6f (white oval), PSI (white rectangle), and TpDSP1 (black circle). LEF and CEF are indicated by arrows. The thickness and size of the components are representative of protein abundance (measured by quantitative immunoblots) and the magnitude of electron flow (measured by ECS or fluorometry). (*B*) Quantification of relative units of DSP protein in replete and Fe-limited WT cultures. Mean ± SD of three biological replicates is shown with a representative immunoblot.

homologs. Rather, we hypothesize that DSPs are distinct members of a larger family of proton gradient regulator proteins, which includes PGR5 and PGRL1. Unlike PGR5, DSPs contain an ~70-aa insertion (Fig. S5) that encompasses the predicted pair of EF-hand motifs and implicates DSPs in a Ca^{2+}-dependent pathway. DSPs also contain a predicted transmembrane segment (Fig. S1*A*), presumably anchoring it to the thylakoid membrane. However, a recent study in *T. pseudonana* did not find TpDSP1 enriched in the thylakoid membrane proteome (27), suggesting that the hydrophobic region identified in silico may not represent an actual transmembrane segment. PGR5 also does not contain a transmembrane segment but associates with the thylakoid membrane through the membrane-associated PGRL1 protein (23). PGRL1 was recently proposed to be the elusive ferrodoxin-plastoquinone reductase responsible for transferring electrons from PSI to plastoquinone during CEF (28). Although PGRL1 does not itself share sequence similarity to PGR5 or DSP, it was found in *Chlamydomonas reinhardtii* to play roles in maintaining levels of key components of the photosynthetic apparatus as well as mediating CEF around PSI under Fe limitation (29). Notably, CEF in *C. reinhardtii* is Ca^{2+}-dependent and involves a multiprotein complex comprised of PGRL1 and a chloroplast-localized Ca^{2+} sensor (30). Together, these observations lend support to the notion that the plastid-localized Ca^{2+}-binding DSPs play a role in mediating CEF in red plastid-derived organisms.

In a previous study, we showed that Fe limitation induces DSP gene expression in *T. pseudonana* (11), but here, there was no significant change in CEF in WT under Fe limitation (Fig. 2*D*). To determine if increased DSP gene expression translated into higher protein levels, we used immunoblot analysis to monitor the levels of endogenous DSP expression in WT cultures. Although TpDSP1 protein was expressed under replete conditions, expression levels increased within 3 d of the shift to Fe-free media (Fig. 3*B*). However, the increase was modest (~1.4-fold) compared with the 9-fold induction in transcript abundance previously observed under similar conditions (11). This difference not only confirms a disconnect between mRNA and protein levels for some stress-related genes in *T. pseudonana* (31) but also shows that cellular control of DSP is at the posttranscriptional or posttranslational level and that analysis of transcript level alone is insufficient to assess DSP activity. The modest increase in DSP protein levels in WT during Fe limitation also suggests that the benefits of overexpression may be constrained by an associated cost that serves to regulate DSP expression.

Given previous findings of light-regulated expression of *ScDSP1* (12) and the observation that light becomes colimiting at low Fe concentrations due to an increased requirement for Fe-containing photosynthetic proteins, we hypothesized that the cost associated with overexpressing TpDSP1 may be related to the cells' ability to cope with changes in its light regime. To test this idea, we measured the steady-state growth rates of WT, TpDSP1-GFP (i.e., clone 18–58), and clones 18–31 and 18–53 under replete nutrient conditions and irradiances ranging from 25 to 2,000 μmol photons m^{-2} s^{-1} (Fig. 4 and Fig. S6). At growth irradiance levels below 600 μmol photons m^{-2} s^{-1}, μ for WT and TpDSP1-GFP was similar (Fig. 4*A* and Fig. S6*A*). In contrast, light levels ≥ 1,000 μmol photons m^{-2} s^{-1} significantly reduced μ in TpDSP1-GFP compared with WT (Fig. 4*A* and Fig. S6*A*), with respective μ/μ_{max} decreasing 75% and 37% at 2,000 μmol photons m^{-2} s^{-1} (Fig. 4*A*). Because TpDSP1-GFP expression is driven off the light-harvesting complex containing fucoxanthin protein 9 promoter, we wanted to confirm that TpDSP1-GFP expression in the overexpression clone lines was maintained at each of the irradiance levels. GFP fluorescence intensity (as determined by flow cytometry) has been used as a quantitative reporter of gene expression (32), and our own observations that GFP fluorescence intensity correlated well with TpDSP1-GFP protein levels (Fig. 1 *A* and *B*) provided confidence in its use as a real-time proxy for expression. GFP fluorescence levels were not significantly different at growth irradiances > 100 μmol photons m^{-2} s^{-1} (Fig. S6*C*). At the lower light intensities (<100 μmol photons m^{-2} s^{-1}), however, there was a slight decrease in fluorescence, suggesting lower overexpression at these levels. Given that the impaired growth rates were observed at the highest intensities where TpDSP1-GFP was being expressed, we

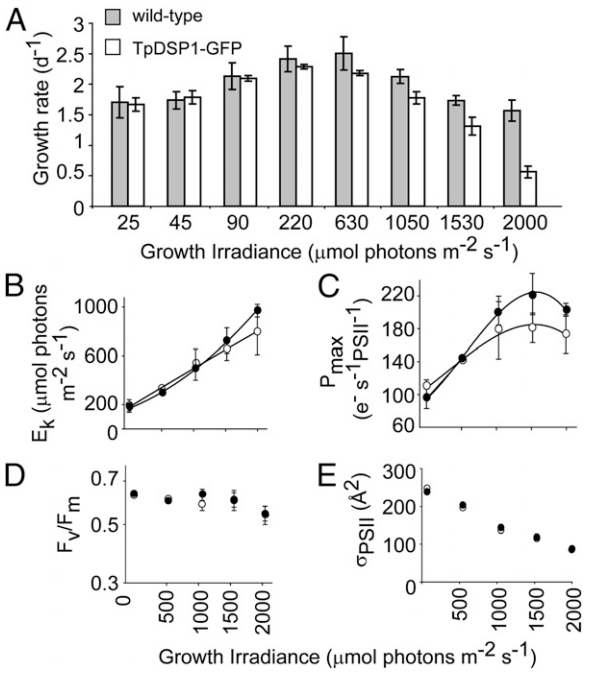

Fig. 4. Growth rate and photosynthetic parameters as a function of irradiance. WT (gray bars and closed symbols) and TpDSP1-GFP (white bars and open symbols) cultures were kept optically thin and acclimated to each irradiance level in nutrient replete medium. (*A*) Specific growth rate. (*B*) Optimal irradiance for photosynthesis (E_k). (*C*) Maximal photosynthetic electron transport rate (P_{max}). (*D*) F_v/F_m. (*E*) Functional cross-section of PSII (σ_{PSII}). The means ± SDs of at least four and three measurements for growth rates and photosynthetic data, respectively, are shown. For clarity, data for clones 18–31 and 18–53 are shown in Fig. S6.

hypothesized that overexpression of TpDSP1 either prevented cells from efficiently photoacclimating or led to a defect in photosynthesis at saturating light. Neither E_k (Fig. 4*B*) nor σ_{PSII} (Fig. 4*E*) was significantly different between WT and TpDSP1-GFP, indicating equal efficiency of photoacclimation. F_v/F_m was also similar at saturating light (Fig. 4*D*), further verifying that there was no effect on PSII. However, P_{max} was significantly lower (Fig. 4*C* and Fig. S6*B*), and nonphotochemical quenching was higher (0.54 ± 0.04 vs. 0.25 ± 0.04 in WT) in TpDSP1-GFP at 2,000 μmol photons m^{-2} s^{-1}, supporting the hypothesis that overexpression of TpDSP1 indeed impaired photosynthesis at high light. This sensitivity to high light is in contrast to findings that overexpression of PGR5 conferred increased resistance to high light (33), further showing that, although DSP and PGR5 are related, they do possess distinct functions that may stem from the divergence of the red plastid lineage after the secondary endosymbiotic event.

Our results demonstrate that TpDSP1 is regulated by a complex system involving Fe and light. Although its overexpression allows cells to thrive during short periods of Fe limitation by facilitating higher levels of PS components and CEF, its benefits are balanced by an inherent cost of increased susceptibility to high light. Although we cannot elucidate the exact mechanism of DSP, we can provide a few possible scenarios. We note that TpDSP1 has several potential phosphorylation sites (Fig. S7). One possible mechanism, implied by the sensitivity of the overexpression clones to high light and the localization of the protein to the plastid, is that TpDSP1 may undergo reversible, redox-regulated phosphorylation (34, 35) that would allow the protein to form a supercomplex with PSI and cytochrome b_6f (36), thereby increasing the kinetic flux of electrons through CEF. This scenario would effectively allow DSP, like PGRL1, to act as a flux valve between CEF and LEF (28, 29). Alternatively or perhaps, in conjunction with phosphorylation, it has also been suggested that diatoms transduce Fe stress signals through a Ca^{2+}-based regulatory system (37). The EF-hand in DSP may, therefore, play a role in a signal transduction cascade triggered by low Fe but regulated by light through phosphorylation. Regardless, the effect of TpDSP1, operating in conjunction with other Fe-responsive pathways and associated genes (7, 10, 11), ultimately leads to elevated fitness under Fe stress and shows that overexpression of a single protein can modulate photosynthetic electron flow and alleviate Fe stress in a diatom.

DSP-like sequences were identified in the genomes of the diatoms *P. tricornutum* and *F. cylindrus* as well as the coccolithophore *E. huxleyi* (Fig. 5), but were absent from the prasinophyte *Ostreococcus tauri*, the primitive Rhodophyte *Cyanidioschyzon merolae*, and the nonphotosynthetic stramenopile *Phytophthora*, further supporting their role in photosynthesis in diverse phytoplankton from secondary endosymbiotic red plastid lineages. In silico analysis predicts plastid localization of DSP proteins in *P. tricornutum* and *S. costatum* but not *E. huxleyi* or *F. cylindrus*. These results may simply be mispredictions associated with the in silico analysis or, if they indeed represent true cytoplasmic localizations, could suggest an additional, undetermined role for DSPs. Additional experiments in other species are needed to determine if the role of TpDSP1 is broadly distributed. Notably, DSP-like sequences were widely distributed in metagenomic and metatranscriptomic datasets from the oligotrophic Sargasso Sea, the California Coastal Upwelling System, the Southern Ocean, and the Equatorial Pacific (Fig. 5 and Dataset S1) as well as the chronically Fe-limited surface waters at Ocean Station Papa in the northeast Pacific Ocean (38). Phylogenetic analyses revealed that environmental DSP-like sequences clustered into distinct groups along with diatom and coccolithophore reference genomes (Fig. 5). Together with our functional genomics data, these findings highlight the relevance of this protein to phytoplankton populations in the modern ocean. We hypothesize that, in the dynamic coastal environment where cells are exposed to varying levels of Fe and light availability on short timescales, cells expressing DSP under subsaturating light would be biochemically poised to cope with Fe stress through elevated CEF and therefore, have a competitive advantage. However, the fact that elevated DSP levels led to impaired photosynthetic rates at saturating light forces cells to walk an ecological tightrope through the regulation of this protein.

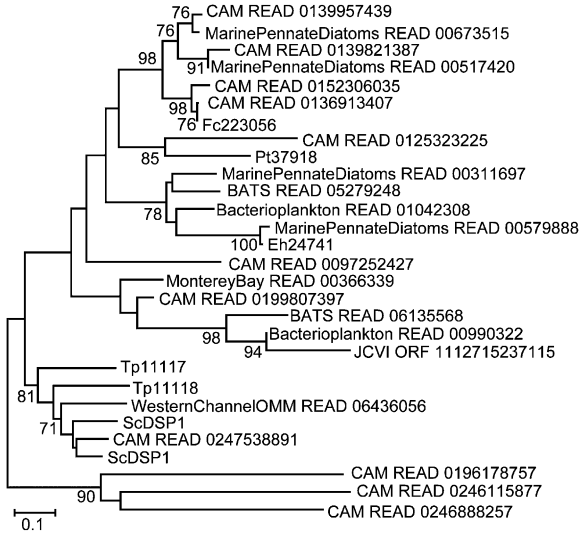

Fig. 5. Phylogenetic relationship of TpDSP1-like proteins. Twenty-eight TpDSP1-like sequences were obtained from genomic sequences and metagenomic and metatranscriptomic libraries. A phylogenetic tree based on an alignment of ~90 aa was obtained using the Neighbor-Joining method. The percentage of replicate trees in which the associated taxa clustered together in the bootstrap test (>70% for 2,000 replicates) is shown next to the branch, with the scale bar representing the number of amino acid substitution per site. Protein IDs are shown for *T. pseudonana* (Tp), *P. tricornutum* (Pt), *F. cylindrus* (Fc), and *E. huxleyi* (Eh). Additional information is in Dataset S1.

Materials and Methods

Culture Conditions. Axenic *T. pseudonana* (Hasle et Heimdale clone 3H; CCMP1335), obtained from the Provasoli–Guillard National Center for Marine Algae and Microbiota, was maintained in enriched seawater, artificial water (ESAW) medium at 18 °C under 120 μmol photons m^{-2} s^{-1} continuous light (supplied by F17T8/Triten50 bulbs). For acute Fe limitation, replete cultures were harvested and washed in Fe-free ESAW and then resuspended in Fe-free ESAW. For chronic, steady-state, low-Fe acclimated growth, cultures were grown in Aquil medium. Fe-EDTA was added as 1:1.1 mM $FeCl_3$:Na_2EDTA to final total Fe concentrations of 52, 102, and 602 nmol L^{-1}. For steady-state, light-acclimated growth, optically thin (<3 × 10^5 cells mL^{-1}) replete cultures were transferred every 1–2 d until growth rates did not vary for at least three consecutive measurements. Desired irradiance levels were obtained by varying the distance of the culture from the light source. Additional details are described in *SI Materials and Methods*.

Cloning and Overexpression of TpDSP1. The gene encoding TpDSP1 was cloned into the expression vector pTpfcp (39), generating a C-terminal fusion to GFP. This vector, along with an antibiotic selection vector, was introduced into WT *T. pseudonana* using a Biolistic PDS-1000/He System (Bio-Rad) as described in *SI Materials and Methods*. Positive clones were selected in the presence of antibiotic and screened for GFP fluorescence by flow cytometry and epifluorescence microscopy. Quantitative RT-PCR and immunoblot analysis using a GFP antibody were used to confirm TpDSP1 overexpression.

Biophysical Measurements. ECS spectra were measured using a Joliot-type spectrophotometer (JTS-10; Biologic). Active PSII:PSI ratios were calculated based on the flash-induced ECS signal in the absence and presence of 3-(3,4-dichlorophenyl)-1,1-dimethylurea and hydroxylamine. CEF was calculated from a linear fit of the initial slope of the ECS decrease normalized to the flash-induced ECS increase in PSII-inhibited cells (i.e., one charge separation

PSI^{-1}) after the light was turned off. Photosynthetic characteristics of PSII were measured using a custom-built Fluorescence Induction and Relaxation System (40), providing measurements of F_o (minimum) and F_m (maximum) fluorescence yields and the functional absorption cross-section of PSII (σ_{PSII}). Maximum efficiency of PSII was calculated as $F_v/F_m = (F_m - F_o)/F_m$. Non-photochemical quenching was calculated as $(F_m - F_m')/F_m'$. Photosynthetic electron transport rates (P_{max}) and the light saturation irradiance (E_k) were retrieved by fitting photosynthesis vs. irradiance curves with the exponential rise function $P = P_{max}(1 - \exp(E/E_k))$. Functional cross-sections of PSI (σ_{PSII}) were measured using photoaucoustics (41). Additional details are in *SI Materials and Methods*.

Elemental and Chl Contents, Absorption Cross-Section Measurements, and Calculation of Quantum Requirement. Carbon and nitrogen contents were measured on a CHN Analyzer (Carlo Erba Instruments). Chl was extracted in 90% (vol/vol) acetone and determined spectrophotometrically. In vivo absorption spectra were measured with an SLM-Aminco DW-2000 Spectrophotometer (375- to 750-nm scan) using live cultures. The wavelength-specific cross-section (a*) of optical absorption normalized to Chl *a* and the quantum yield for growth were calculated using these values and are described in *SI Materials and Methods*.

Amino Acid Alignments and Phylogenetic Tree Construction. These methods are described in *SI Materials and Methods* along with Protein ID and GenBank accession numbers.

ACKNOWLEDGMENTS. We thank N. Kröger and N. Poulsen for providing overexpression vectors and advice on transformations. We also thank I. Grouneva and E.-M. Aro for access to their thylakoid membrane proteome dataset. C. Gardner assisted with confocal microscopy, flow cytometery was done by F. Natale, C. Fuller performed CHN analysis, M. Maniscalco assisted with quantitative RT-PCR, M. Sebastian helped with phylogenetic analysis, and M. Chu performed fluorescence/cell density calibrations experiments. This study was supported by an Institute of Marine and Coastal Sciences Postdoctoral Fellowship (to K.T.), National Science Foundation Grants OCE-0927829 (to K.D.B.) and 0927733 (to A.B.K.) and, in part, by the Gordon and Betty Moore Foundation through Grant GBMF3789 (to K.D.B.).

1. Kolber ZS, et al. (1994) Iron limitation of phytoplankton photosynthesis in the equatorial Pacific Ocean. *Nature* 371(6493):145–149.
2. Boyd PW, et al. (2007) Mesoscale iron enrichment experiments 1993–2005: Synthesis and future directions. *Science* 315(5812):612–617.
3. Hutchins DA, DiTullio GR, Zhang Y, Bruland KW (1998) An iron limitation mosaic in the California upwelling regime. *Limnol Oceanogr* 43(6):1037–1054.
4. Kustka AB, Allen AE, Morel FM (2007) Sequence analysis and transcriptional regulation of iron acquisition genes in two marine diatoms. *J Phycol* 43(4):715–729.
5. Marchetti A, Maldonado MT, Lane ES, Harrison PJ (2006) Iron requirements of the pennate diatom *Pseudo-nitzschia*: Comparison of oceanic (high-nitrate, low-chlorophyll waters) and coastal species. *Limnol Oceanogr* 51(5):2092–2101.
6. Marchetti A, et al. (2009) Ferritin is used for iron storage in bloom-forming marine pennate diatoms. *Nature* 457(7228):467–470.
7. Allen AE, et al. (2008) Whole-cell response of the pennate diatom *Phaeodactylum tricornutum* to iron starvation. *Proc Natl Acad Sci USA* 105(30):10438–10443.
8. Strzepek RF, Harrison PJ (2004) Photosynthetic architecture differs in coastal and oceanic diatoms. *Nature* 431(7009):689–692.
9. Valdez-Holguin JE, Alvarez-Borrego S, Mitchell BG (1998) Photosynthetic parameters of phytoplankton in the California Current system. *Calcofi Rep* 39:148–158.
10. Mock T, et al. (2008) Whole-genome expression profiling of the marine diatom *Thalassiosira pseudonana* identifies genes involved in silicon bioprocesses. *Proc Natl Acad Sci USA* 105(5):1579–1584.
11. Thamatrakoln K, Korenovska O, Niheu AK, Bidle KD (2012) Whole-genome expression analysis reveals a role for death-related genes in stress acclimation of the diatom *Thalassiosira pseudonana*. *Environ Microbiol* 14(1):67–81.
12. Chung C-C, Hwang S-PL, Chang J (2005) Cooccurrence of ScDSP gene expression, cell death, and DNA fragmentation in a marine diatom, *Skeletonema costatum*. *Appl Environ Microbiol* 71(12):8744–8751.
13. Chung C-C, Hwang S-PL, Chang J (2008) Nitric oxide as a signaling factor to upregulate the death-specific protein in a marine diatom, Skeletonema costatum, during blockage of electron flow in photosynthesis. *Appl Environ Microbiol* 74(21):6521–6527.
14. Gschloessl B, Guermeur Y, Cock JM (2008) HECTAR: A method to predict subcellular targeting in heterokonts. *BMC Bioinformatics* 9:393.
15. Emanuelsson O, Nielsen H, von Heijne G (1999) ChloroP, a neural network-based method for predicting chloroplast transit peptides and their cleavage sites. *Protein Sci* 8(5):978–984.
16. Emanuelsson O, Brunak S, von Heijne G, Nielsen H (2007) Locating proteins in the cell using TargetP, SignalP and related tools. *Nat Protoc* 2(4):953–971.
17. Westerlund I, Von Heijne G, Emanuelsson O (2003) LumenP—a neural network predictor for protein localization in the thylakoid lumen. *Protein Sci* 12(10):2360–2366.
18. Apt KE, et al. (2002) *In vivo* characterization of diatom multipartite plastid targeting signals. *J Cell Sci* 115(Pt 21):4061–4069.
19. Gruber A, et al. (2007) Protein targeting into complex diatom plastids: Functional characterisation of a specific targeting motif. *Plant Mol Biol* 64(5):519–530.
20. Kilian O, Kroth PG (2005) Identification and characterization of a new conserved motif within the presequence of proteins targeted into complex diatom plastids. *Plant J* 41(2):175–183.
21. Brown C, et al. (2008) Flux capacities and acclimation costs in *Trichodesmium* from the Gulf of Mexico. *Mar Biol* 154(3):413–422.
22. Munekage Y, et al. (2002) PGR5 is involved in cyclic electron flow around photosystem I and is essential for photoprotection in *Arabidopsis*. *Cell* 110(3):361–371.
23. DalCorso G, et al. (2008) A complex containing PGRL1 and PGR5 is involved in the switch between linear and cyclic electron flow in *Arabidopsis*. *Cell* 132(2):273–285.
24. Munekage Y, et al. (2004) Cyclic electron flow around photosystem I is essential for photosynthesis. *Nature* 429(6991):579–582.
25. Arnon DI, Allen MB, Whatley FR (1954) Photosynthesis by isolated chloroplasts. *Nature* 174(4426):394–396.
26. Allen JF (2003) Cyclic, pseudocyclic and noncyclic photophosphorylation: New links in the chain. *Trends Plant Sci* 8(1):15–19.
27. Grouneva I, Rokka A, Aro E-M (2011) The thylakoid membrane proteome of two marine diatoms outlines both diatom-specific and species-specific features of the photosynthetic machinery. *J Proteome Res* 10(12):5338–5353.
28. Hertle AP, et al. (2013) PGRL1 is the elusive ferredoxin-plastoquinone reductase in photosynthetic cyclic electron flow. *Mol Cell* 49(3):511–523.
29. Petroutsos D, et al. (2009) PGRL1 participates in iron-induced remodeling of the photosynthetic apparatus and in energy metabolism in *Chlamydomonas reinhardtii*. *J Biol Chem* 284(47):32770–32781.
30. Terashima M, et al. (2012) Calcium-dependent regulation of cyclic photosynthetic electron transfer by a CAS, ANR1, and PGRL1 complex. *Proc Natl Acad Sci USA* 109(43):17717–17722.
31. Dyhrman ST, et al. (2012) The transcriptome and proteome of the diatom *Thalassiosira pseudonana* reveal a diverse phosphorus stress response. *PLoS One* 7(3):e33768.
32. Soboleski MR, Oaks J, Halford WP (2005) Green fluorescent protein is a quantitative reporter of gene expression in individual eukaryotic cells. *FASEB J* 19(3):440–442.
33. Long TA, Okegawa Y, Shikanai T, Schmidt GW, Covert SF (2008) Conserved role of proton gradient regulation 5 in the regulation of PSI cyclic electron transport. *Planta* 228(6):907–918.
34. Escoubas JM, Lomas M, LaRoche J, Falkowski PG (1995) Light intensity regulation of *cab* gene transcription is signaled by the redox state of the plastoquinone pool. *Proc Natl Acad Sci USA* 92(22):10237–10241.
35. Pfannschmidt T, Nilsson A, Allen JF (1999) Photosynthetic control of chloroplast gene expression. *Nature* 397(6720):625–628.
36. Iwai M, et al. (2010) Isolation of the elusive supercomplex that drives cyclic electron flow in photosynthesis. *Nature* 464(7292):1210–1213.
37. Falciatore A, d'Alcalà MR, Croot P, Bowler C (2000) Perception of environmental signals by a marine diatom. *Science* 288(5475):2363–2366.
38. Marchetti A, et al. (2012) Comparative metatranscriptomics identifies molecular bases for the physiological responses of phytoplankton to varying iron availability. *Proc Natl Acad Sci USA* 109(6):E317–E325.
39. Poulsen N, Chesley PM, Kröger N (2006) Molecular genetic manipulation of the diatom *Thalassiosira pseudonana* (Bacillariophyceae). *J Phycol* 42(5):1059–1065.
40. Gorbunov MY, Falkowski PG (2005) Fluorescence Induction and Relaxation (FIRe) technique and instrumentation for monitoring photosynthetic processes and primary production. *Photosynthesis: Fundamental Aspects to Global Perspectives: Proceedings of the 13th International Congress on Photosynthesis*, eds Van der Est A, Bruce D (Allen and Unwin, London), pp 1029–1031.
41. Yan C, et al. (2011) Photosynthetic energy storage efficiency in *Chlamydomonas reinhardtii*, based on microsecond photoacoustics. *Photosynth Res* 108(2–3):215–224.

Supporting Information

Thamatrakoln et al. 10.1073/pnas.1304727110

SI Materials and Methods

Cloning of *Thalassiosira pseudonana* Death-Specific Protein 1 Gene for Overexpression. *T. pseudonana* death-specific protein 1 (*TpDSP1*), a gene with a 936-bp ORF and no predicted introns, was amplified from genomic DNA by PCR based on the available genome sequence of TpDSP1 (http://genome.jgi-psf.org/Thaps3/Thaps3.home.html; protein ID Thaps_11118). TpDSP1 was cloned into the EcoRV/KpnI site of the expression vector pTpfcp (1), which was provided by Nils Kröger (Technische Universität, Dresden, Germany), generating a C-terminal fusion to GFP. The construct pTpfcp-DSP1, hereafter referred to as TpDSP1-GFP, containing a modified linker, TSAAAA, between the TpDSP1 and EGFP gene encoding regions was used, because it was previously shown to enhance GFP folding in eukaryotes (2). The sequence and frame were confirmed by sequencing both strands of the construct (Genewiz Inc.).

Microparticle Bombardment and Screening of Transformants. pTpfcpDSP1-GFP was cotransformed with the antibiotic selection vector, pTpfcpNAT (provided by N. Kröger, Technische Universität, Dresden, Germany) into *T. pseudonana* cells using the Biolistic PDS-1000/He system (Bio-Rad) as previously described (1). Briefly, 5 μg both pTpfcp-DSP and pTpNAT were coated onto sterilized M17 tungsten particles using the $CaCl_2$-spermidine method according to the manufacturer's protocol (Bio-Rad). Approximately 1×10^8 of *T. pseudonana* cells were plated on enriched seawater, artificial water (ESAW) plates containing 1.5% agar and allowed to air dry. Cells were bombarded with the DNA-coated tungsten particles at 1,550 psi, and then, they were immediately scraped into liquid ESAW media and incubated overnight under constant illumination (120 μmol photons m^{-2} s^{-1}). To select for positive transformants, 5×10^6 cells were embedded in ESAW plates containing 0.3% agarose and 100 μg mL^{-1} antibiotic nourseothricin (Werner BioAgents) under constant light until colonies were observed. Individual colonies were picked into 24-well plates containing 1.5 mL ESAW with 100 μg mL^{-1} nourseothricin. Clones were initially screened by epiflourescence microscopy using an IX71 Inverted Microscope (Olympus) and GFP Filter (Chroma Technology Corp) or an InFlux Model 209S Mariner Flow Cytometer (BD Biosciences) at 520 nm after excitation with a 488-nm laser. Gating and data analyses were performed using FlowJo analytical software (Tree Star Inc.). GFP-positive clones were further confirmed by harvesting cells by centrifugation (10 min at 12,000 × *g*) and resuspending in either 20 μL Lyse-*N*-Go (Pierce) for PCR analysis or 2% SDS for immunoblot analysis. Quantitative RT-PCR was performed using DSP-specific primers and the Brilliant SYBR Green QPCR Core Reagent Kit and MX3000P System (Stratagene) according to the manufacturer's protocol. Stock cultures of positive transformants were maintained in ESAW + 100 μg/mL nourseothricin under continuous light and transferred every 7–10 d. Confocal microscopy was performed using a Leica TCS SP5 spectral confocal microscope at Rutgers' Analytical Cytometry/Image Analysis Core Facility Environmental and Occupational Health Sciences Institute/Cancer Institute of New Jersey.

Immunoblot Analysis. Quantitative immunoblots were performed as previously described (3). Briefly, 250–500 μL 1× lysis buffer of 0.5 mmol L^{-1} EDTA, 140 mM Tris base, 105 mM Tris·HCl, 10% Glycerol, and 2% lithium dodecyl sulfate were added to pellets, and samples were frozen in liquid nitrogen and sonicated (Misonix; power setting of two to three). After a second round of freezing and sonication, samples were centrifuged at 20,000 × *g* at 4 °C for 5 min. Protein concentrations were determined using a DC Protein Assay Kit (Bio-Rad). Equal protein amounts (0.6 μg total protein) were loaded onto TGX 4–20% gradient gels (Bio-Rad). Proteins were transferred to PVDF and blocked in 1× Tris-buffered saline with Tween 20 (Tris-buffered saline (TBS) containing 0.2% Tween-20 (vol/vol) (TBST)) and 2% ECL Advance Blocking Reagent (GE Healthcare). Primary antibodies (Agrisera) were used at dilutions of 1:40,000 for RuBisCO (RbcL), photosystem II (PSII; PsbD), cytochrome b_6f (PetC), and ATP synthase (AtpB) and 1:10,000 for PSI (PsaC), and they were developed using ECL Advance (GE Healthcare) and an HRP-conjugated secondary antibody (1:10,000 dilution; Agrisera). Blots were washed after each incubation with two quick rinses in 1× TBST (0.2%) followed by three washes for 5 min each. Images of immunoblots were obtained using a CCD imager (Chemidoc XRS+; Bio-Rad). Protein levels were quantitated as previously described (3) using Quantity One software (Bio-Rad). Adjusted volume values were obtained, and standard curves were used to estimate the amount of protein in experimental samples. Recombinant proteins used for standard curves have been previously described (3).

Protein samples for GFP and TpDSP1 immunoblot analyses were obtained as described above. Equal protein amounts (3 μg total protein for GFP and 5 μg total protein for TpDSP1) were loaded onto TGX 4–20% gradient gels (Bio-Rad). Proteins were transferred to PVDF, blocked in 1× TBST and 2% ECL Advance Blocking Reagent (GE Healthcare), and then washed in 1× TBST. GFP primary antibody was purchased from AbCam and used at a 1:2,000 dilution. A synthetic peptide based on the TpDSP1 amino acid sequence (EAPKTLKVNLVKLAKNNGGD) was used to generate a polyclonal antibody, which was tested for specificity and is now commercially available (AS10 935; Agrisera). Anti-TpDSP1 was used at a 1:10,000 dilution.

Acute and Chronic Iron Limitation Experiments. For acute nitrogen or Fe limitation experiments, WT and TpDSP1-GFP cells were grown in ESAW (4) to a cell density of 1–1.5 × 10^6 cells mL^{-1}. Cells were then harvested by filtration onto 0.8-μm filters using 13-mm Swinnex filter holders (Millipore), washed in N- or Fe-free ESAW, and resuspended in acid-washed glassware in replete ESAW or N- or Fe-free ESAW medium at a cell density of 1.5×10^5 cells mL^{-1}. Cell abundance was determined using a Coulter Multisizer II (Beckman Coulter) fitted with a 70-μm orifice. Coulter Counter measurements were also used to determine the average equivalent spherical diameter to calculate cell volume using the equation $V = 4/3\pi r^3$. Eight independent experiments were done, each containing two to three biological replicates. After 2–3 d in Fe-free medium, when the growth rate was statistically different between WT and TpDSP1-GFP, cells were harvested by filtration, and cell pellets were stored at −80 °C until processed. For chronic, steady-state low Fe acclimated growth, cultures were grown in Aquil medium (5) containing metals and macronutrients as described previously (6) in 28-mL polycarbonate tubes. Natural abundance Fe-EDTA stock was prepared from $FeCl_3$ and Na_2EDTA (1:1.1 mM), whereas a radiolabeled ^{59}Fe-EDTA stock was prepared from $^{59}FeCl_3$ (NEZ037001MCI; Perkin-Elmer) and Na_2EDTA (50:55 μM). Media were prepared with total Fe concentrations of 52, 102, and 602 nmol L^{-1}, assuming 2 nM background Fe. The corresponding Fe′ values of 361, 708, and 4,180 pM were calculated

(5), assuming a pH of 8.3. Fe was added to media from the ^{59}Fe-EDTA stock to achieve a total activity of 16,500–33,000 Bq L^{-1} media, with the balance of Fe supplied from the natural abundance Fe-EDTA stock. Cells were grown under 24 h light at 360 μmol photon m^{-2} s^{-1} and 18 °C. Relative in vivo chlorophyll fluorescence was measured daily on a Turner Designs AU-10 fluorometer, and specific growth rate was calculated from the relationship between time and natural log of fluorescence. Cells were transferred to new growth media during midexponential growth (at an initial density of ∼140 cells mL^{-1}) before fluorescence values corresponding to a cell density of 4×10^5 cells mL^{-1} were exceeded. Cells were maintained under steady-state conditions for at least two transfers (corresponding to >22 generations) before sampling for metal quota. Total ^{59}Fe activity was determined by removing 200 μL into 7-mL scintillation vials, and the remaining volume of each tube (determined gravimetrically) was filtered onto a pair of 47-mm 3-μm polycarbonate filters and rinsed with an oxalate-EDTA solution (7, 8). The bottom filter served as a blank correction for any nonspecific ^{59}Fe adsorption, which was minor (90% of blanks were ≤14% of the signal). Filters were placed in 7-mL scintillation vials, Eco-Scint scintillation mixture was added, and activity was determined on a Beckman Coulter LSC6500 scintillation counter. Quota was calculated relative to fluorescence readings at the time of harvest and then converted to cellular quotas based on the relationship between in vivo fluorescence and cell density. This relationship was determined from Coulter Counter-based cell counts of simultaneous cultures grown without radiolabel (in the same incubator under identical conditions). Steady-state Fe uptake rates were determined as the products of steady-state growth rate and Fe quota (9). Growth rates, Fe quotas, and uptake rates were determined from $n = 4$, 6, and 7 cultures of WT grown under calculated Fe′ of 361, 708, and 4,180 pM Fe′, respectively and from $n = 4$, 6, and 4 cultures of TpDSP1-GFP under the same conditions. Error bars represent SE.

Steady-State Light-Acclimated Growth. Replete cultures were maintained optically thin ($<3 \times 10^5$ cells mL^{-1}) to prevent self-shading and nutrient limitation. Flow cytometry analysis of GFP fluorescence was used to confirm that TpDSP1-GFP was expressed at each of the light irradiances. Growth rates were calculated based on measurements of cell concentration and maximum fluorescence (F_m), which were in close agreement with each other. Cultures were illuminated using either white or blue light-emitting diodes.

Determining Quantum Requirement for Growth. Carbon and nitrogen contents were obtained from cells harvested on precombusted GF/F filters and an Na 1500 Series 2 CHN Analyzer (Carlo Erba Instruments). Chlorophyll concentrations were calculated as described (10). The efficiency of transduction of light energy at a given irradiance intensity into chemical energy (total carbon) was calculated with a simplified version of the model by Falkowski et al. (11), where the quantum yield for growth (φ_μ; expressed in moles C per moles quanta absorbed) was calculated from the equation

$$\varphi_\mu = \frac{\mu}{a^* \times (\text{Chl } a/\text{C}) \times I_\mu \times 1{,}040},$$

where μ is the growth rate ($days^{-1}$), a* is the in vivo absorption cross-section [$meters^2$ $milligrams^{-1}$ chlorophyll a (Chl a)], Chl *a* and C are the biomasses (milligrams) of Chl a and total cell carbon, respectively, I_μ is the growth irradiance (micromoles quanta $meters^{-2}$ $seconds^{-1}$), and 1,040 is a constant used to convert from micromoles quanta $meters^{-2}$ $seconds^{-1}$ to moles quanta $meters^{-2}$ $days^{-1}$ and from milligrams C to moles C. The quantum requirement (moles quanta per mole C) was obtained by taking the inverse of φ_μ ($1/\varphi_\mu$).

Biophysical Measurements. Electrochromic shift (ECS) measurements were made on a JTS-10 spectrophotometer. When required, the PSII chemical inhibitors 3-(3,4-dichlorophenyl)-1, 1-dimethylurea (DCMU) and hydroxylamine (HA) were used at final concentrations of 15 μM and 1 mM, respectively. Cells were harvested, concentrated 10-fold by filtration, and resuspended in ESAW medium supplemented with Ficoll 10% (wt/vol) to avoid sedimentation. Cells were dark-acclimated for at least 30 min before measuring at room temperature with a Joliot-type spectrophotometer (JTS-10; Biologic). The light minus dark ECS signals in WT were measured at each wavelength between 450 and 600 nm 500 ms after a saturating laser flash. Given that the two main peaks of the ECS spectrum (∼525 and 555 nm) corresponded to the maxima in the oxidized minus reduced c-type cytochromes spectra, we used 513 nm in this study to avoid any contribution of cytochromes to the ECS signals. The ECS signal obtained shortly (130 μs) after a saturating flash is proportional to the number of flash-induced charge separations within reaction centers (i.e., the total number of PSs in the sample). Conversely, the signal obtained on addition of DCMU and HA is proportional to the number of PSI only (review in ref. 12). Active PSII:PSI ratios were, thus, calculated based on the ECS signal measured in the absence and presence of DCMU and HA. Cyclic electron flow (CEF) was calculated from a linear fit of the initial slope of the ECS decrease (i.e., 1 charge separation PSI^{-1}) after the light was turned off. Rates of CEF around PSI were determined by inhibiting the activity of PSII with DCMU and HA. Under these conditions, the buildup of the electric field relies solely on CEF around PSI. After a steady-state baseline proton gradient is reached in the light (340 μmol photons m^{-2} s^{-1}), the slope of the ECS signal in the dark represents the rate of CEF-related proton transport in the light (review in ref. 12). Fluorescence-based measurements were done using a Fluorescence Induction and Relaxation System. The minimum (F_o) and maximum (F_m) fluorescence yields, the quantum efficiency of photochemistry in PSII [$F_v/F_m = (F_m - F_o)/F_m$ for dark-adapted cells and $\Delta F'/F_m'$ under ambient light], and the functional absorption cross-section of PSII (σ_{PSII}) were calculated from the analysis of fluorescence induction at microsecond timescale. Nonphotochemical quenching (NPQ), the portion of thermally dissipated photons, was calculated as $NPQ = (F_m - F_m')/F_m'$. The photosynthesis vs. irradiance curves were reconstructed from measurements of electron transport rates ($P = E \times \sigma_{PSII} \times \Delta F'/F_m'$) as a function of ambient irradiance (E) in the range from 0 to 2,000 μmol quanta m^{-2} s^{-1}. The maximum rates of photosynthetic electron transport (P_{max}) and the light saturation irradiance (E_k) were retrieved by fitting the photosynthesis vs. irradiance curves with the exponential rise function, $P = P_{max}(1 - \exp(E/E_k))$. The functional cross-sections of PSI (σ_{PSII}) were measured using a microsecond time-resolved photoacoustic instrument (13) as previously described (14).

Environmental Sequences and Generation of Phylogenetic Tree. Environmental and genomic sequences were identified using TBLASTN with TpDSP1 as the query. Environmental sequences were obtained from CAMERA using the "All metagenomic ORFs from Sanger" and "All metagenomic 454 reads" databases with an e cutoff of $<10^{-4}$. Reciprocal BLASTX, using a cutoff e value $< 10^{-11}$ and the nr database, was performed to confirm that sequences had highest similarity to DSP. In addition, each of the sequences was predicted to contain an EF-hand motif, further supporting their similarity to DSP. Pairwise comparisons between TpDSP1 and environmental/genomic sequences ranged between 30% and 73% amino acid identity. Samples obtained from water filtered with <1-μm filters as well as redundant se-

quences were manually removed. The remaining 22 environmental sequences were trimmed to ~90 aa and aligned along with 7 sequences from published genomes using ClustalW (15). MEGA5 (16) was used to generate a Neighbor-Joining tree. The evolutionary distances were computed using the Poisson correction method. All ambiguous positions were removed for each sequence pair. Names indicated in Fig. 5 are unique identifiers obtained from CAMERA; more information can be found in Dataset S1.

Protein ID and GenBank Accession Numbers. Protein IDs from sequenced genomes were: DSPs, 11118 (TpDSP1) and 11117 (TpDSP2), 223056 (*Fragilariopsis cylindrus*), 37918 (*Phaeodactylum tricornutum*), 424741 (*Emiliania huxleyi*); Tp proton gradient regulator-5 (TpPGR5; 22396), PtPGR5 (34248), EhPGR5 (61309), and FcPGR5 (222477). GenBank accession numbers were AAY27742 [*Skeletonema costatum* DSPs (ScDSP1)], EF590267 (ScDSP2), AtPGR5 (*Arabidopsis thaliana*; NP_565327), PopTri (*Populus trichocarpa*; XP_002314501), GmPGR5 (*Glycine max*; NP_001241362), OsPGR5 (*Oryza sativa*; NP_001062542), ZmPGR5 (*Zea mays*; NP_001151447), CrPGR5 (*Chlamydomonas reinhardtii*; XP_001700905), and OtPGR5 (*Ostreococcus tauri*; XP_003082569).

1. Poulsen N, Chesley PM, Kröger N (2006) Molecular genetic manipulation of the diatom *Thalassiosira pseudonana* (Bacillariophyceae). *J Phycol* 42(5):1059–1065.
2. Chang H-C, Kaiser CM, Hartl FU, Barral JM (2005) De novo folding of GFP fusion proteins: High efficiency in eukaryotes but not in bacteria. *J Mol Biol* 353(2): 397–409.
3. Brown C, et al. (2008) Flux capacities and acclimation costs in *Trichodesmium* from the Gulf of Mexico. *Mar Biol* 154(3):413–422.
4. Harrison PJ, Waters RE, Taylor FJR (1980) A broad specturm artificial medium for coastal and open ocean phytoplankton. *J Phycol* 16(1):28–35.
5. Sunda WG, Price NM, Morel FM (2005) Trace metal ion buffers and their use in culture studies. *Algal Culturing Techniques*, ed Andersen RA (Elsevier, Amsterdam), pp 35–63.
6. Kustka AB, Allen AE, Morel FM (2007) Sequence analysis and regulation of iron acquisition genes in two marine diatoms. *J Phycol* 43(4):715–729.
7. Tang D, Morel FMM (2006) Distinguishing between cellular and Fe-oxide-associated trace elements in phytoplankton. *Mar Chem* 98(1):18–30.
8. Tovar-Sanchez A, et al. (2003) A trace metal clean reagent to remove surface-bound iron from marine phytoplankton. *Mar Chem* 82(1–2):91–99.
9. Sunda WG, Huntsman SA (1995) Iron uptake and growth limitation in oceanic and coastal phytoplankton. *Mar Chem* 50(1–4):189–206.
10. Jeffrey SW, Humphrey GF (1975) New spectrophotometric equations for determining chlorophylls a, b, c1 and c2 in higher plants, algae, and natural phytoplankton. *Biochem Physiol Pflanz* 167:191–194.
11. Falkowski PG, Dubinsky Z, Wyman K (1985) Growth-irradiance relationships in phytoplankton. *Limnol Oceanogr* 30(2):311–321.
12. Bailleul B, et al. (2010) An atypical member of the light-harvesting complex stress-related protein family modulates diatom responses to light. *Proc Natl Acad Sci USA* 107(42):18214–18219.
13. Yan C, et al. (2011) Photosynthetic energy storage efficiency in *Chlamydomonas reinhardtii*, based on microsecond photoacoustics. *Photosynth Res* 108(2–3):215–224.
14. Charlebois DO, Mauzerall DC (1999) Energy storage and optical cross-section of PSI in the cyanobacterium *Synechococcus* PCC 7002 and a psaE- mutant. *Photosynth Res* 59(1):27–38.
15. Thompson JD, Higgins DG, Gibson TJ (1994) CLUSTAL W: Improving the sensitivity of progressive multiple sequence alignment through sequence weighting, position-specific gap penalties and weight matrix choice. *Nucleic Acids Res* 22(22):4673–4680.
16. Tamura K, et al. (2011) MEGA5: Molecular evolutionary genetics analysis using maximum likelihood, evolutionary distance, and maximum parsimony methods. *Mol Biol Evol* 28(10):2731–2739.

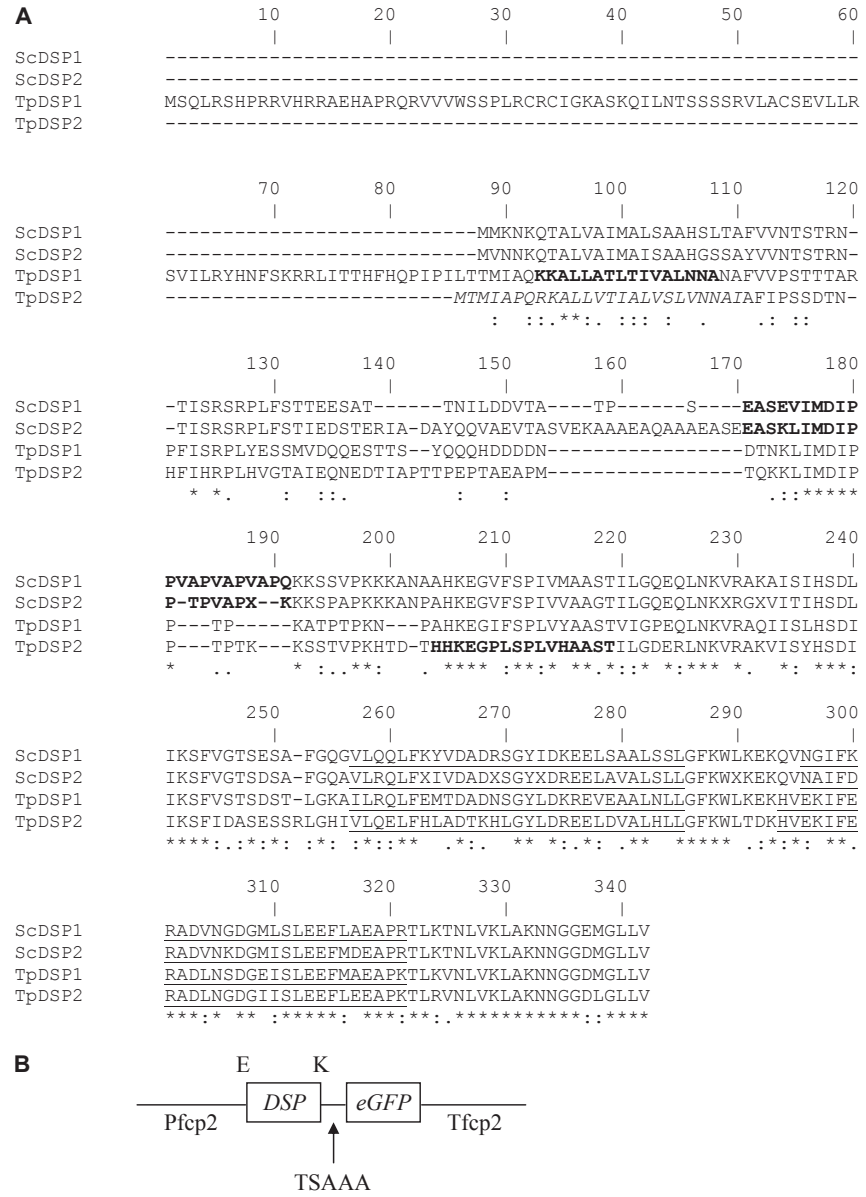

Fig. S1. Bioinformatic analysis of DSP proteins and map of the expression construct used for overexpressing TpDSP1-GFP. (*A*) Amino acid alignment using ClustalW (1) of DSP proteins from *T. pseudonana* and *S. costatum*. Asterisks denote identical residues, and colons and periods represent strongly and weakly similar residues, respectively. TpDSP1 and TpDSP2 sequences are based on gene models with Expressed Sequence Tag support for both the 5′ and 3′ ends. Using SignalP 3.0 (2), TpDSP2 was predicted to contain a signal peptide (italics). Transmembrane segments are shown in bold and were predicted for TpDSP1 and TpDSP2 using MEMSAT-SVM (3) or previously reported for ScDSP1 and ScDSP2 (4). EF-hands are underlined and were predicted using CD-Search (5) and ScanProsite (6) for TpDSP1 and TpDSP2 or as previously reported (4). (*B*) Map of TpDSP1-GFP fusion construct. *TpDSP1* was cloned into the *Eco*RV (E) and KpnI (K) sites of the plasmid pTpfcp (7), producing an in-frame C-terminal fusion with EGFP separated by a 5-aa linker (TSAAA). Expression of the fusion protein was regulated by the promoter (Pfcp2) and terminator (Tfcp2) for the fucoxanthin Chl *a*/*c* 9 binding protein *LHCF9*).

1. Thompson JD, Higgins DG, Gibson TJ (1994) CLUSTAL W: Improving the sensitivity of progressive multiple sequence alignment through sequence weighting, position-specific gap penalties and weight matrix choice. *Nucleic Acids Res* 22(22):4673–4680.
2. Emanuelsson O, Brunak S, von Heijne G, Nielsen H (2007) Locating proteins in the cell using TargetP, SignalP and related tools. *Nat Protoc* 2(4):953–971.
3. Nugent T, Jones DT (2009) Transmembrane protein topology prediction using support vector machines. *BMC Bioinformatics* 10(1):159.
4. Chung C-C, Hwang S-PL, Chang J (2005) Cooccurrence of ScDSP gene expression, cell death, and DNA fragmentation in a marine diatom, *Skeletonema costatum*. *Appl Environ Microbiol* 71(12):8744–8751.
5. Marchler-Bauer A, Bryant SH (2004) CD-Search: Protein domain annotations on the fly. *Nucleic Acids Res* 32(Web Server Issue):W327–W331.
6. de Castro E, et al. (2006) ScanProsite: Detection of PROSITE signature matches and ProRule-associated functional and structural residues in proteins. *Nucleic Acids Res* 34(Web Server Issue):W362–W365.
7. Poulsen N, Chesley PM, Kröger N (2006) Molecular genetic manipulation of the diatom *Thalassiosira pseudonana* (Bacillariophyceae). *J Phycol* 42:(5)1059–1065.

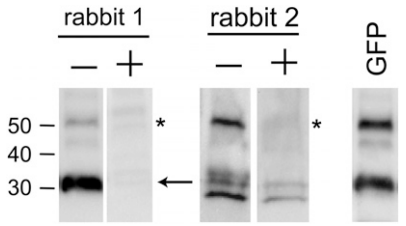

Fig. S2. DSP immunoblot analysis and peptide competition assay. Protein extracts from nutrient replete grown cultures of TpDSP1-GFP were probed with the DSP antibody (–) or the DSP antibody after preincubation with the antigenic peptide (+) from two rabbits. Rabbit 1 cross-reacted preferentially and specifically with endogenous DSP (arrow), with slight cross-reactivity to the TpDSP1-GFP fusion protein (asterisk), whereas rabbit 2 preferentially cross-reacted with the fusion protein (asterisk). Nonspecific binding in the region of endogenous DSP (i.e., those interactions not competed away in the peptide competition assay) precluded using rabbit 2 antiserum for detecting endogenous DSP. The blot probed with rabbit 1 antiserum was reprobed with a GFP antibody (GFP blot), further confirming that DSP and GFP antibodies differentially detected TpDSP-GFP1. The ~32-kDa band in the GFP blot is residual signal from the DSP antibody and does not represent cross-reactivity with the GFP antibody.

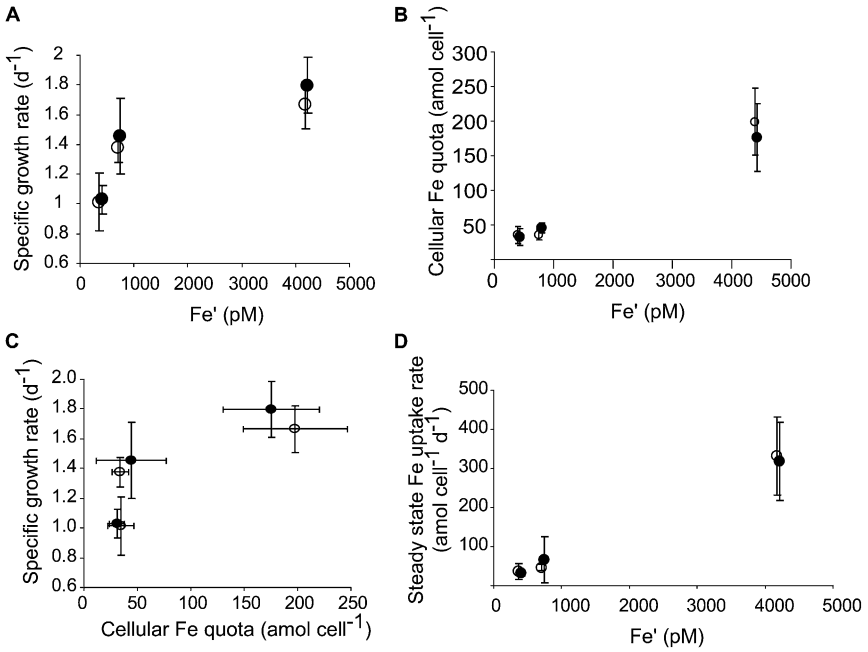

Fig. S3. Interrelationships of Fe′, cellular Fe quota, growth, and Fe uptake for WT (closed circles) and TpDSP1-GFP (open circles) grown under steady-state conditions. (*A*) Specific growth rate vs. Fe′. (*B*) Cellular Fe quota vs. Fe′. (*C*) Specific growth rate vs. cellular Fe quota. (*D*) Steady-state Fe uptake rate vs. Fe′. WT Fe′ values in *A*, *C*, and *D* are offset by +20 pM for clarity. Error bars indicate SE calculated from $n = 4$, 6, and 7 cultures from WT grown under calculated Fe′ of 361, 708, and 4,180 pM Fe′, respectively, and from $n = 4$, 6, and 4 cultures of TpDSP1-GFP under the same conditions.

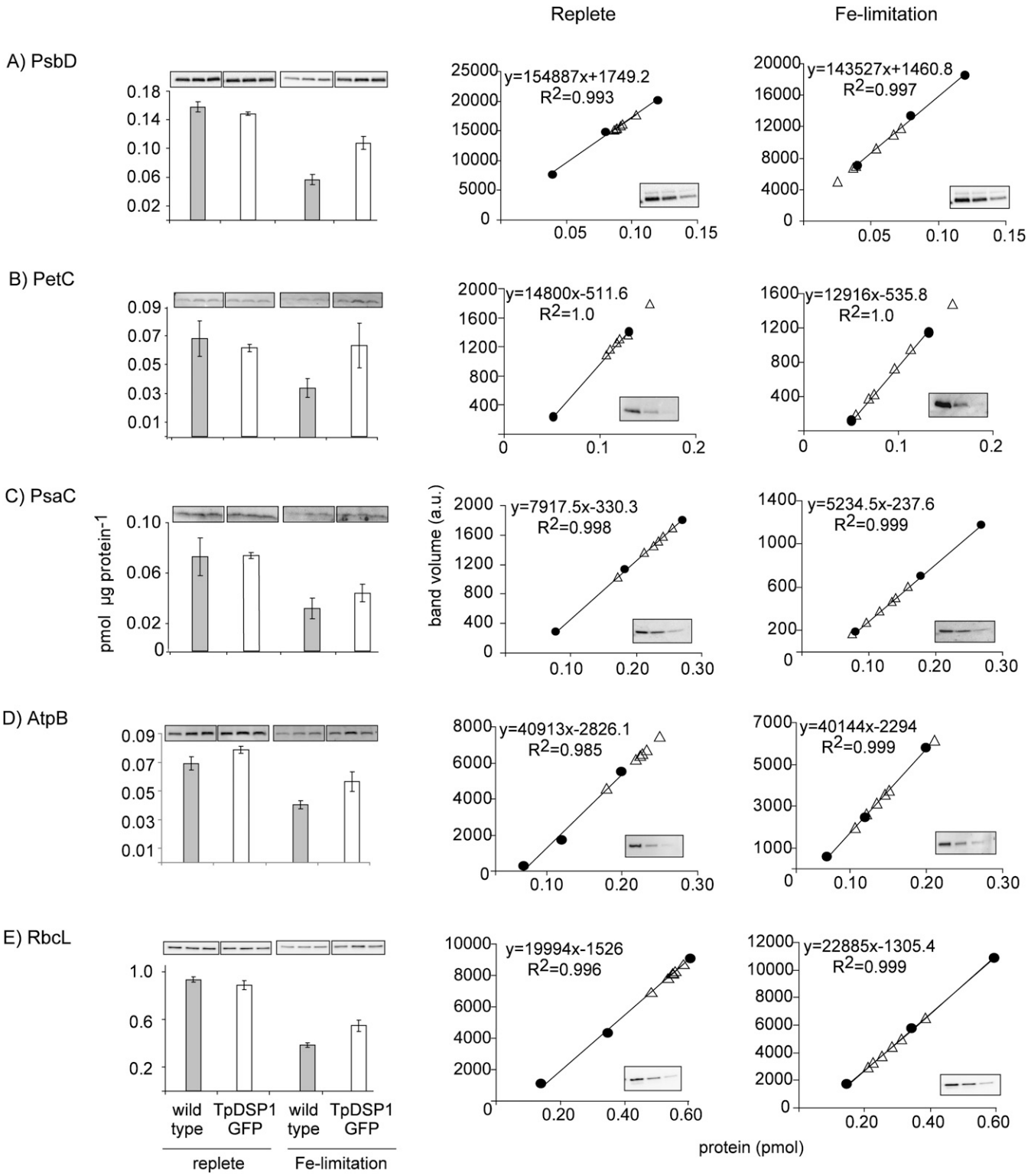

Fig. S4. Quantitative immunoblots and corresponding standard curves. (*Left*) Quantification of proteins for replete and Fe-limited WT and TpDSP1-GFP is shown in the bar graphs: (*A*) PsbD (PSII), (*B*) PetC (Cyt b_6f), (*C*) PsaC (PSI), (*D*) AtpB (ATP synthase), and (*E*) RbcL (RuBisCO). Mean of triplicate cultures with SD is shown. Immunoblot images for each culture are shown above each respective bar graph. Quantification (picomoles micrograms protein^{-1}) was based on standard curves of respective recombinant proteins in replete (*Center*) and Fe-limited (*Right*) cultures. In each case, a linear relationship was observed for protein levels spanning several orders of magnitude (closed circles, standards; open triangles, experimental samples). The equations used to calculate protein levels are shown along with R^2 values. (*Insets*) Immunoblots showing the relative detection signal of serially diluted, purified recombinant protein standards.

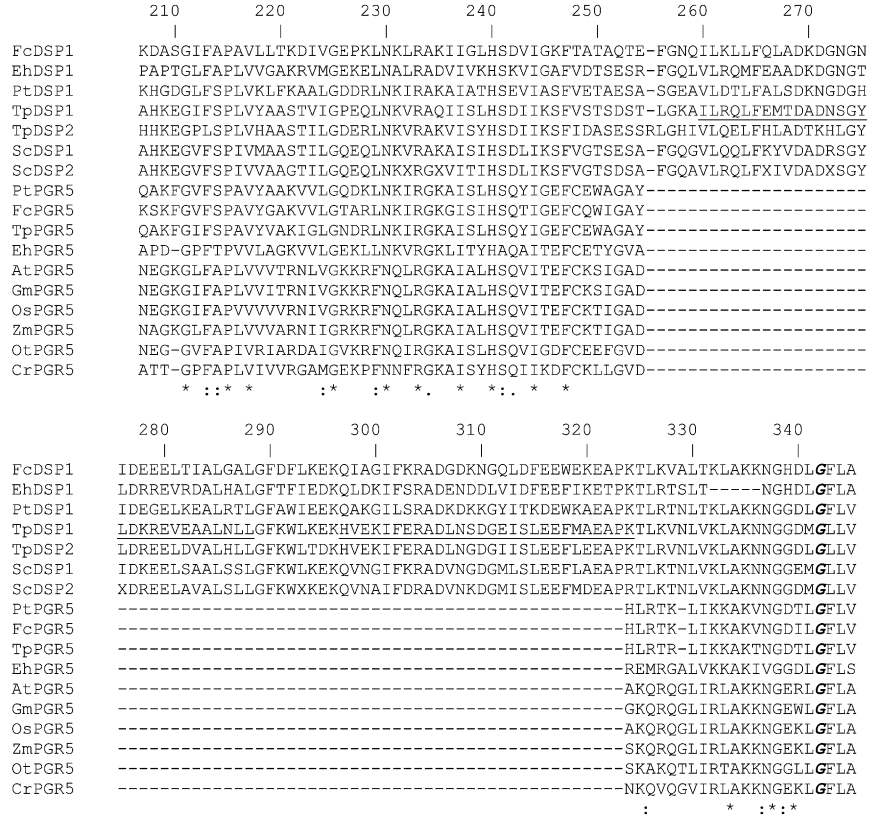

Fig. S5. Multiple sequence alignment of partial DSP and PGR5 proteins. Amino acid alignment was generated using ClustalW (1). Numbering represents amino acid position based on TpDSP1. DSP proteins range in total size from 188 to 311 aa, whereas PGR5 proteins are 90–141 aa in total length. Asterisks denote identical residues, and colons and periods represent strongly and weakly similar residues, respectively. The underlined portion of TpDSP1 represents the predicted pair of EF-hand motifs. The essential and conserved glycine residue is shown in bold and italics (position 343), respectively. Abbreviations, protein IDs, and GenBank accession numbers are in *SI Methods and Materials*.

1. Thompson JD, Higgins DG, Gibson TJ (1994) CLUSTAL W: Improving the sensitivity of progressive multiple sequence alignment through sequence weighting, position-specific gap penalties and weight matrix choice. *Nucleic Acids Res* 22(22):4673–4680.

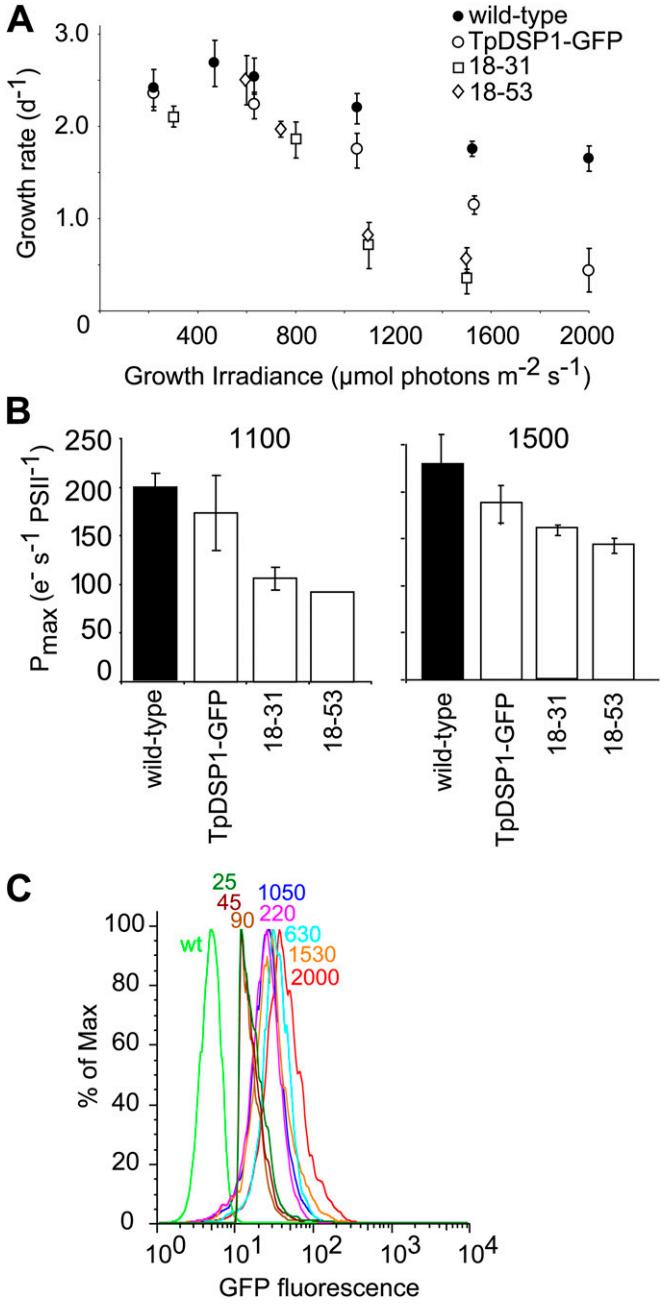

Fig. S6. Growth rate, photosynthesis, and TpDSP1-GFP expression measurements as a function of growth irradiance. Note: Data from Fig. 4 for WT and TpDSP1-GFP are shown for comparison. (*A*) Specific growth rate for WT (closed circles), TpDSP1-GFP (open circles), clone 18–31 (squares), and clone 18–53 (diamonds). Cultures were kept optically thin in nutrient replete medium and acclimated to each respective irradiance level until stable growth rates were obtained. Data represent the means and SDs of at least three measurements, except for 18–53 grown at 1,100 μmol photons m^{-2} s^{-1}, which is a single data point. (*B*) Maximal photosynthetic electron transport rate (P_{max}) for cultures acclimated to a growth irradiance of 1,100 or 1,500 μmol photons m^{-2} s^{-1}. Data are the means and SDs of at least two measurements, except for 18–53 at 1,100 μmol photons m^{-2} s^{-1}, which is a single measurement. (*C*) GFP fluorescence intensity obtained by flow cytometry for TpDSP1-GFP after acclimation to the indicated irradiance levels. Colored numbers represent the respective growth irradiance in micromoles photons meters^{-2} seconds^{-1}; the fluorescence of WT culturesis provided for comparison. Percent of max is a normalized representation of the number of events as determined by FlowJo (Tree Star Inc.). Histograms are representative of at least two measurements. For simplicity, only data for TpDSP1-GFP are shown, but clones 18–31 and 18–53 showed similar intensities at a subset of irradiance levels.

```
MSQLRSHPRRVHRRAEHAPRQRVVVWSSPLRCRCIGKASKQILNTSSSSRVLACSEVLLRSVILRYHNFSKRRLITTHFH      80
QPIPILTTMIAQKKALLATLTIVALNNANAFVVPSTTTARPFISRPLYESSMVDQQESTTSYQQQHDDDDNDTNKLIMDI     160
PPTPKATPTPKNPAHKEGIFSPLVYAASTVIGPEQLNKVRAQIISLHSDIIKSFVSTSDSTLGKAILRQLFEMTDADNSG     240
YLDKREVEAALNLLGFKWLKEKHVEKIFERADLNSDGEISLEEFMAEAPKTLKVNLVKLAKNNGGDMGLLV              320
.................................................S.....................S.........      80
......T.............................T.........Y..S..........Y...................     160
..T...T.T.....................................................ST.....................S.     240
Y................................S....S..........T....................                  320

Phosphorylation sites predicted:  Ser: 7   Thr: 7   Tyr: 3
```

Fig. S7. Putative phosphorylation sites in TpDSP1. In silico prediction was performed using NetPhos 2.0 (1). TpDSP1 amino acid sequence is shown followed by the localization of the predicted phosphorylation sites.

1. Blom N, Gammeltoft S, Brunak S (1999) Sequence and structure-based prediction of eukaryotic protein phosphorylation sites. *J Mol Biol* 294(5):1351–1362.

Other Supporting Information Files

Dataset S1 (XLS)
Table S1 (DOC)